Electronic Supplementary Material (ESI) for Materials Horizons.
This journal is © The Royal Society of Chemistry 2018

Electronic Supplementary Information:

Electron tunneling through grain boundaries in transparent conductive oxides and implications for electrical conductivity: the case of ZnO:Al thin films

Viet Huong Nguyen*[,a,b], Ulrich Gottlieb[a], Anthony Valla[b], Delfina Muñoz[b], Daniel Bellet[a] and David Muñoz-Rojas*[,a]

[a]*Univ. Grenoble Alpes, CNRS, Grenoble INP, LMGP, F-38000 Grenoble, France*

[b]*Univ. Grenoble Alpes, CEA, LITEN, INES, F-73375, Le Bourget-du-Lac, France*

Table of contents

1. Sample preparation and characterization 2
2. Validity of (Wentzel–Kramers–Brillouin) WKB approximation 2
3. Calculation of tunneling transfer matrix 4
4. Effect of grain size on carrier transport 6
5. Parameters used for conductivity modeling 9
6. Effect of C, K, and N_t to the fits 9

References 11

1. Sample preparation and characterization

ZnO:Al samples were deposited on borosilicate glass substrates by using different deposition techniques: ALD, AP-SALD and sputtering. For the films prepared with our AP-SALD home-made system, diethylzinc ($(C_2H_5)_2Zn$; DEZ, Aldrich), trimethylaluminum ($(CH_3)_3Al$; TMA, Aldrich) and water vapor were used as precursors for zinc, aluminum, and oxygen, respectively. The substrate temperature was maintained at 200 °C. The samples were maintained at the distance of 150 µm from the gas injector and oscillated under the injector at 10 cm/s to deposit over a maximum area of 5 cm x 5 cm. More details about this deposition technique can be found in our previous works.[1,2] The as-deposited samples prepared by AP-SALD showed a low mobility (< 1 $cm^2V^{-1}s^{-1}$) because of adsorbed oxygen at grain boundaries during deposition in atmospheric conditions, which limits electron transport through grain boundaries.[3–5] In our work, we performed a post-deposition treatment of the AP-SALD samples under vacuum at 200 °C for 1 h. During the treatment, the samples were subjected to UV light (wavelength: 365 nm, power: 15 W, distance between sample and light source: 15 cm) to reduce the oxygen trap density at the grain boundary of ZnO doped films, as reported in previous investigations.[3,6,7] For the films prepared by the ALD technique, we used a TFS 500 system with the same type of precursors. The deposition temperature was set at 200 °C while the pressure in the deposition chamber was maintained at 1 mbar. For the films prepared by DC sputtering, the system Jusung 7003–Soultera with a sputtering power of 200 W was used. A target containing 2% Al_2O_3 and 98% ZnO was used. The depositions were carried out at 200 °C in a pure Argon atmosphere.

The surface morphology of different films was analyzed by scanning electron microscopy (SEM-FEG Environmental FEI QUANTA 250) and atomic force microscopy (AFM Digital Instruments Dimension 3100). Atomic structure and crystallinity were studied by X-ray diffraction (XRD, Bruker D8 Advance) in Bragg-Brentano configuration; using Cu-Kα radiation (λ= 0.15406 nm) in the 2θ range of 20°−80° (0.011°/step, 2 s/step). Transmission electron microscopy (TEM) images were obtained using a JEOL JEM-2010 microscope operating at 200 kV. Hall mobility and carrier concentration were analyzed by using a home-made Hall Effect analyzer with a magnetic field strength of 5000 G and temperature control from 30 K to 300 K by using a liquid helium cryostat. During Hall Effect measurements, the samples were kept at a pressure of 0.003 mbar.

The structural analysis including AFM, SEM, XRD, and TEM show that ZnO:Al samples prepared by the AP-SALD technique have a high crystallinity with a mean grain size of 46 nm for a 205 nm-thick film (see Figure 3 below and the associated discussion). Since the AFM technique allows only accessing the biggest grains on the top of the films, therefore, the mean grain size used for our mobility calculation is estimated to be around one half of the grain size measured by AFM, i.e. 20 nm for a 200 nm thick film.

2. Validity of (Wentzel–Kramers–Brillouin) WKB approximation

The electron wave functions in two neighbor grains can be solved by using the 1D time-independent Schrödinger equation:

$$-\frac{\hbar^2}{2m_n}\frac{\partial^2}{\partial x^2}\Psi(x)+V(x)\Psi(x)=E_x\Psi(x) \tag{1}$$

Where ħ is the reduced Plank constant, Ψ(x) is the electron wave-function and V(x) is the potential energy at the grain boundary. In the case of a constant potential, the solution of the Schrödinger equation can take the form of a simple plane wave: $\Psi(x) = Ae^{ikx}$, where $k = \sqrt{2m_n(E_x - V)}/\hbar$ is a constant. The WKB approximation assumes that if the potential *V(x)* changes slowly with *x*, the wave function solution of the Schrödinger equation are also of the form of simple plane wave: $\Psi(x) = Ae^{iS(x)}$, with $S(x) = xk(x)$.

Replacing this expression to the equation (1), we obtain:

$$i\frac{\partial^2 S(x)}{\partial x^2} - \left(\frac{\partial S(x)}{\partial x}\right)^2 + (k(x))^2 = 0 \tag{2}$$

Because the wave vector *k(x)* is proportional to the square root of the potential *V(x),* which is assumed to be slowly varying. This means that the second derivative of $xk(x) = S(x)$ is negligible compared to $(k(x))^2$, thus we can write:

$$\frac{\partial S(x)}{\partial x} = k(x) \text{ or } S(x) = \int k(x)dx + Cte \tag{3}$$

In the case of tunneling through a grain boundary barrier $V(x) > E_x$, so $k = i\sqrt{2m_n(V(x) - E_x)}/\hbar$ and the wave function can be expressed as:

$$\Psi(x) = K\exp\left(-\int\sqrt{\frac{2m_n(V(x) - E_x)}{\hbar^2}}dx\right) \tag{4}$$

If now we consider an incoming wave Ψ_1 to the grain boundary barrier *V(x)* and a transmitted wave Ψ_2 after passing through the barrier, with two turning points x_1 and x_2 corresponding to the positions where the electron kinetics energy E_x equal to the potential *V(x)*. The tunneling probability is thus given by:

$$\mathrm{T}(\mathrm{E}_x) = \left|\frac{\Psi_2(x_2)}{\Psi_1(x_1)}\right|^2 = -\frac{2}{\hbar}\int_{x1}^{x2}\sqrt{2m_n(V(x) - E_x)}dx \ , \ E_x < V(x) \tag{5}$$

To obtain this expression, we have assumed that the potential varies slowly with x, which is a large assumption in our case of sharp parabolic potential barrier. The variation of the potential is more important for higher doping level. In addition, the W KB approximation breaks down at regions where the electron kinetics energy approaches the potential barrier, which makes the wave vector approaches to zero but its derivative is not. It should be also noted that the WKB assumption leads to a tunneling probability of unity for the electron energies higher than the grain boundary barrier, whereas it should not be as in the quantum-mechanical point of view

3. Calculation of tunneling transfer matrix

We discretized the grain boundary potential barrier into N segments with $N + 1$ equidistant points ($x_1, x_2 ... x_i, x_{i+1} ... x_{N+1}$), where x_1 and x_{N+1} correspond to the bottom of the conduction band on each side. The potential $V(x_i)$ corresponding to each point x_i follows the parabolic solution of the Poisson's equations.

The solutions of the 1D time-independent Schrödinger's equation in the interior of the grains, where the potential is zero, have the plane wave forms:

$$\Psi_L(x) = a_L e^{ik_L x} + b_L e^{-ik_L x}, \quad x < x_1 \tag{6.a}$$

$$\Psi_R(x) = a_R e^{ik_R x} + b_R e^{-ik_R x}, \quad x > x_{N+1} \tag{6.b}$$

where Ψ_L, k_L, k_R, Ψ_R are the wave functions and the wave vectors attributed to the left and right grains. We have neglected the applied bias on one side so that we can write the wave vectors as follows: $k_L = k_R = \sqrt{2m_n E_x} / \hbar$. We assume that $b_R = 0$. The objective of the next part is to calculate the total tunneling probability: $T = \left|\frac{a_R}{a_L}\right|^2$.

The linear function U_i of potential in the segment (x_i, x_{i+1}), $2 \le i \le N$, is expressed as:

$$U_i(x) = K_i.(x - x_i) + V(x_i), \text{ with } K_i = \frac{V(x_{i+1}) - V(x_i)}{x_{i+1} - x_i} \tag{7}$$

In order to use the Airy function solution, we need to adjust the 1D time-independent Schrödinger's equation by changing the variable from x to ξ_i as follows:

$$\xi_i = \left(\frac{2m_i}{\hbar^2} K_i\right)^{\frac{1}{3}} \left(\frac{V(x_i) - E_x}{K_i} + (x - x_i)\right) \tag{8}$$

and the x-independent derivative: $\xi_i^{'} = \left(\frac{2m_i}{\hbar^2} K_i\right)^{\frac{1}{3}}$, where m_i denotes the electron effective mass in the considered region. In a first approximation, we assume that m_i is constant when tunneling through the grain boundary barrier and takes the value of the effective mass at the bottom of the conduction band, m_0.

The 1D time-independent Schrödinger's equation in the segment (x_i, x_{i+1}) can thus be rewritten as:

$$\frac{\partial^2 \Psi_i}{\partial \xi_i^2} - \xi_i \Psi_i = 0 \tag{9}$$

The solution for this type of equation can be expressed as a linear combination of Airy functions, *Ai* and *Bi:*

$$\Psi_i(x) = a_i Ai(\xi_i) + b_i Bi(\xi_i), \quad x_i < x < x_{i+1} \tag{10}$$

The similar solution for the wave function in the neighbor segment (x_{i-1}, x_i) should take the same form, as follows:

$$\Psi_{i-1}(x) = a_{i-1}Ai(\xi_{i-1}) + b_{i-1}Bi(\xi_{i-1}),\ \ x_{i-1} < x < x_i \tag{11}$$

Now the boundary conditions at the interface between two adjacent segments (x_{i-1}, x_i) and (x_i, x_{i+1}) require the continuity of the wave functions, as well as its derivative in the position x_i:

$$\begin{cases} a_i Ai(\xi_i) + b_i Bi(\xi_i) = a_{i-1}Ai(\xi_{i-1}) + b_{i-1}Bi(\xi_{i-1}) & (12) \\ a_i Ai'(\xi_i)\xi_i' + b_i Bi'(\xi_i)\xi_i' = a_{i-1}Ai'(\xi_{i-1})\xi_{i-1}' + b_{i-1}Bi'(\xi_{i-1})\xi_{i-1}' & (13) \end{cases}$$

By using the property of the Airy functions: $Ai(z)Bi'(z) - Ai'(z)Bi(z) = \pi^{-1}$ and then combining the equations (12) and (13) under the matrix form, we obtain:

$$\begin{pmatrix} a_{i-1} \\ b_{i-1} \end{pmatrix} = T_i \begin{pmatrix} a_i \\ b_i \end{pmatrix} \tag{14}$$

Where T_i is transfer matrix related to the electron tunneling process through the segment (x_i, x_{i+1}) and calculated as follows:

$$T_i = \pi \begin{pmatrix} Ai(\xi_i)Bi'(\xi_{i-1}) - Ai'(\xi_i)Bi(\xi_{i-1})\frac{\xi_i'}{\xi_{i-1}'} & Bi(\xi_i)Bi'(\xi_{i-1}) - Bi'(\xi_i)Bi(\xi_{i-1})\frac{\xi_i'}{\xi_{i-1}'} \\ -Ai(\xi_i)Ai'(\xi_{i-1}) + Ai'(\xi_i)Ai(\xi_{i-1})\frac{\xi_i'}{\xi_{i-1}'} & -Bi(\xi_i)Ai'(\xi_{i-1}) + Bi'(\xi_i)Ai(\xi_{i-1})\frac{\xi_i'}{\xi_{i-1}'} \end{pmatrix} \tag{15}$$

Equation (14) is valid only for $i = (2...N-1)$. Similarly, the transfer matrices in the segment (x_1, x_2) and (x_N, x_{N+1}) can be expressed as follows:

$$T_1 = \frac{1}{2} \begin{pmatrix} Ai(\xi_1) + \frac{Ai'(\xi_1)\xi_1'}{ik_L} & Bi(\xi_1) + \frac{Bi'(\xi_1)\xi_1'}{ik_L} \\ Ai(\xi_1) - \frac{Ai'(\xi_1)\xi_1'}{ik_L} & Bi(\xi_1) - \frac{Bi'(\xi_1)\xi_1'}{ik_L} \end{pmatrix} \tag{16}$$

$$T_N = \pi \begin{pmatrix} Bi'(\xi_{N-1}) - \frac{ik_R}{\xi_{N-1}'}Bi(\xi_{N-1}) & Bi'(\xi_{N-1}) + \frac{ik_R}{\xi_{N-1}'}Bi(\xi_{N-1}) \\ -Ai'(\xi_{N-1}) + ik_R Ai(\xi_{N-1}) & -Ai'(\xi_{N-1}) - ik_R Ai(\xi_{N-1}) \end{pmatrix} \tag{17}$$

The total tunneling transfer matrix (called T_{total}) is calculated by multiplying the transfer matrices in each layer (x_i, x_{i+1}), $1 \le i \le N$, which are already calculated and shown in the equations (15), (16) and (17):

$$T_{total} = \frac{\pi^N}{2}\prod_{i=1}^{N} T_i = \begin{pmatrix} T_{11} & T_{12} \\ T_{21} & T_{22} \end{pmatrix} \tag{18}$$

Finally, with the assumption that $b_R = 0$, we obtain the total tunneling probability as follows:

$$T = \left|\frac{a_R}{a_L}\right|^2 = \frac{1}{\left|T_{11}\right|^2} \tag{19}$$

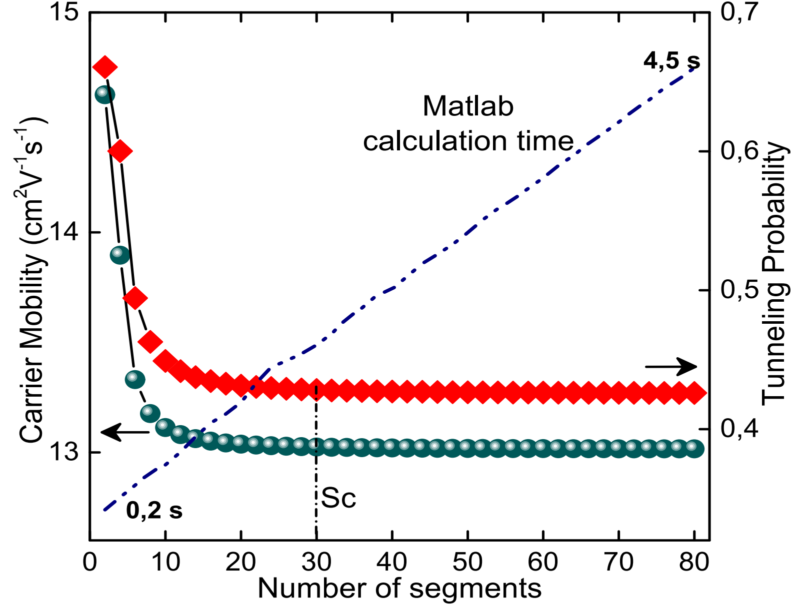

Figure 1: Carrier mobility, tunneling transmission probability, and associated Matlab running time calculated for electrons at the Fermi level as function of the number of segments used for the discretization of the grain boundary potential barrier. $n = 2\times10^{20}$ cm^{-3}, $Nt = 6\times10^{13}$ cm^{-2}, $L = 20$ nm.

Concerning the discretization used for the grain boundary barrier, the larger the number of segments the more accurate the calculated result. However, the calculation time will be also longer. Therefore, we fixed a critical value for the number of segments S_c as follows:

$$\frac{\left|T_{S_c+1} - T_{S_c}\right|}{T_{S_c}} < 0.0001 \tag{20}$$

where T_{Sc} and T_{Sc+1} are the tunneling transmission probability of electrons at the Fermi level, calculated with the AFTMM model by using respectively two numbers of segments: *Sc* and ($S_c + 1$). Figure 1 shows the carrier mobility at 300 K, the tunneling transmission probability and the calculation time as function of the number of segments. When the number of segments varies from 2 to 80, the running time of the model AFTMM to calculate the value of mobility goes from 0.2 s to 4.5 s. By applying the criteria defined above, the critical value *Sc* is determined to be 30, which corresponds to a calculation time of 1.8 s per value. This means that to study the effect of one parameter (temperature, grain size…) on the charge transport through grain boundary, it will only take a few minutes. In this work, we have fixed the number of segments at 30.

4. Effect of grain size on carrier transport

Obviously, if the carrier transport is mainly dominated by ionized impurity scattering, the effect of grain size is not important. However, when grain boundary scattering is one of the main factors limiting the carrier mobility, a high grain boundary density is detrimental for the carrier transport. In order to study the crystalline quality of ZnO:Al films deposited by AP-SALD technique, different

structural analysis techniques were used. Figure 2 shows AFM images of AP-SALD ZnO:Al films deposited at 200 °C with various thicknesses. We observed that the thicker films have the bigger grain size. Figure 3a shows that when increasing film thickness from 205 nm to 525 nm, the mean grain size measured with AFM increases significantly from 46 nm to 69 nm. Since the AFM technique allows only accessing the biggest grains on the top of the films, therefore, we assume that the mean grain size *L* used for our mobility calculation is estimated to be around one half of the grain size measured by AFM, i.e. 20 nm for a 200 nm thick film.

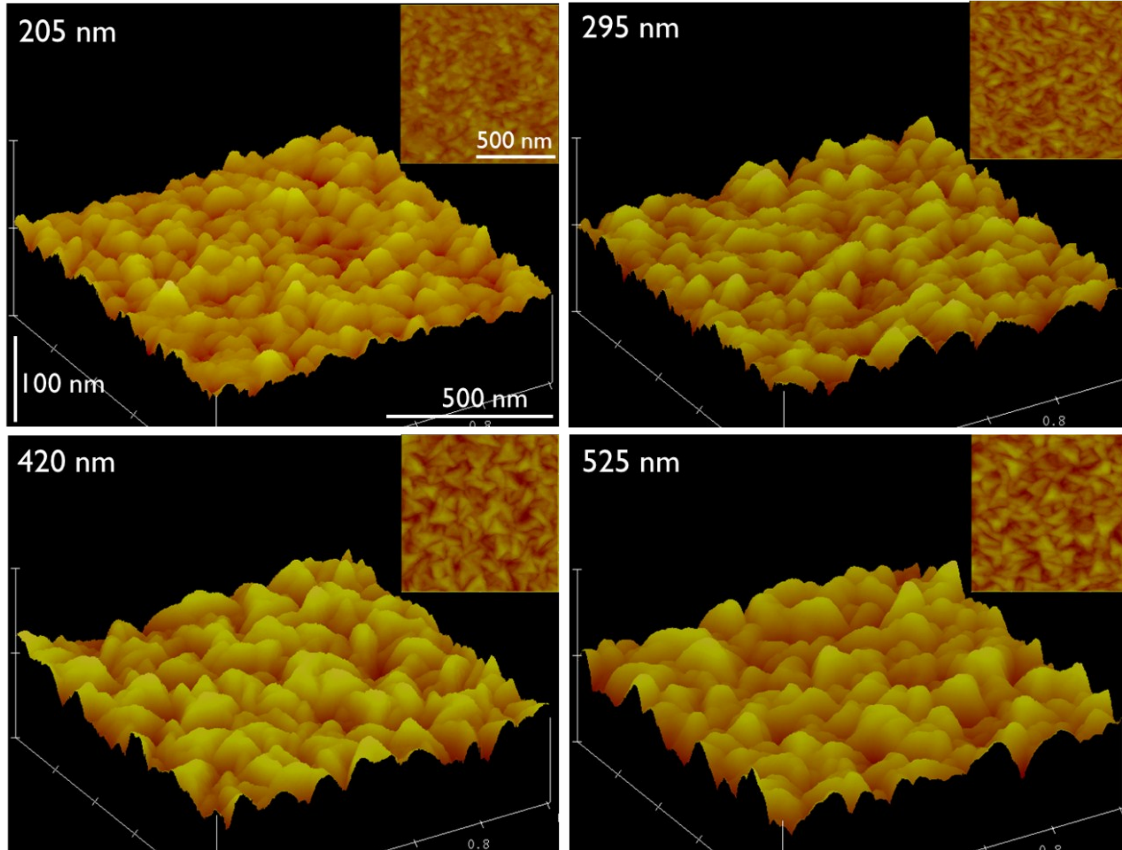

Figure 2: AFM images of AP-SALD ZnO:Al films deposited at 200 °C with various thicknesses, inset: corresponding top-view AFM images.

The XRD patterns of the same set of samples shown in Figure 3b illustrate the same growth orientation for all films. This is again confirmed by the similar surface morphology studied by SEM imaging, as shown in Figure 4.a-d. In addition, Figure 4.e-g show respectively dark-field TEM image, high-resolution TEM images of 500nm-thick ZnO:Al film deposited on Silicon substrate at 200 °C. The XRD, SEM and TEM images clearly show that our films deposited by APSALD technique have a good crystalline quality. Consequently, a low electron mobility in the case of AP-SALD ZnO:Al films should be related to a high electron-trap density at the grain boundaries rather than ingrain scattering.

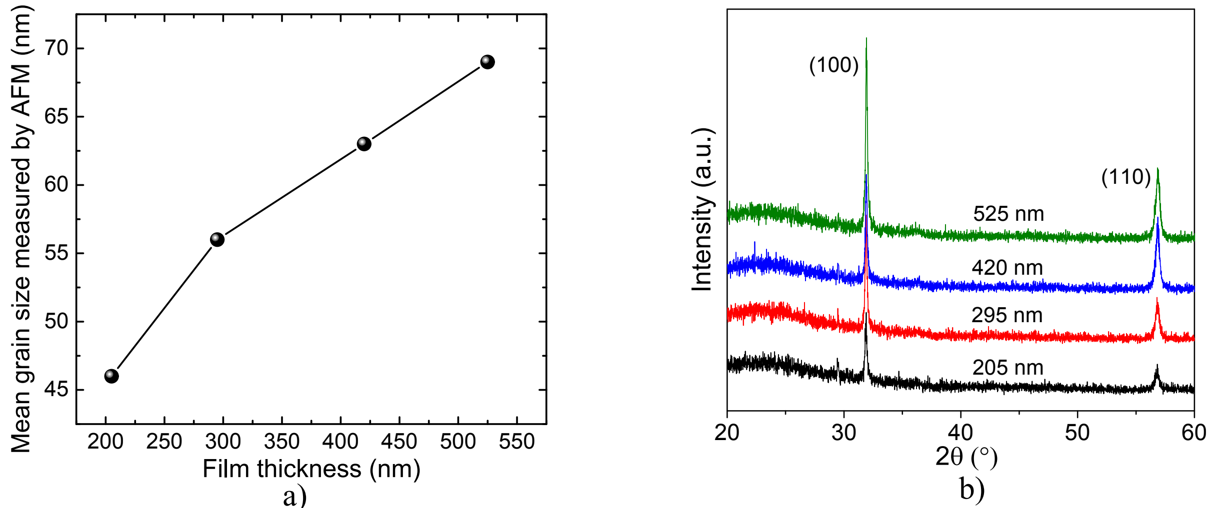

Figure 3 : a) mean grain size measured with AFM and b) X-Ray Diffraction patterns of AP-SALD ZnO:Al films deposited at 200 °C with various thicknesses.

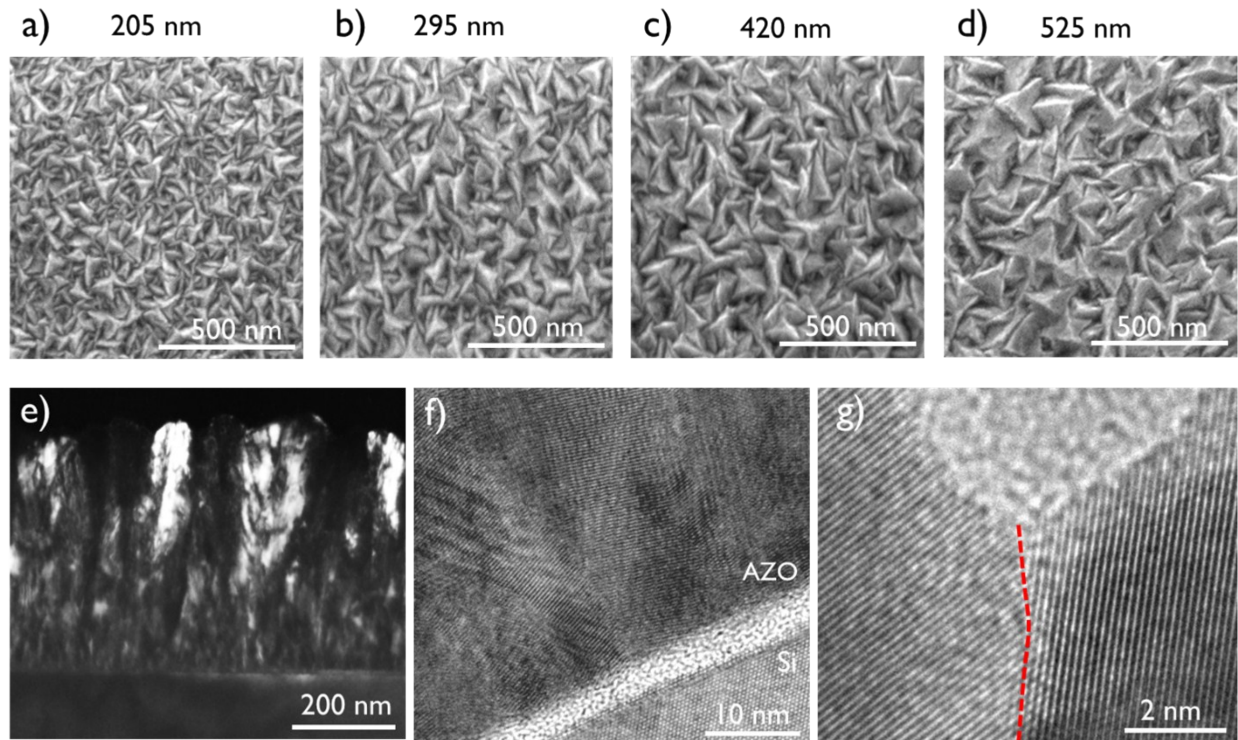

Figure 4 : a-d) SEM micrographs of AP-SALD ZnO:Al films deposited on glass at 200 °C with various thicknesses. e) Dark-field TEM image, f-g) high-resolution TEM images of 500nm-thick ZnO:Al film deposited by AP-SALD on Silicon substrate at 200 °C

Figure 5 shows non-negligible variation of the Hall carrier concentration when the film thickness increases. On the one hand, since N_t depends on the deposition conditions and post-treatment, which are kept the same in this case, the trap density can therefore be assumed to be constant and independent of the grain size. On the other hand, the density of grain boundary is higher in the case of thin films (since average grain size increases for thicker films, as shown by SEM or AFM), and thus in this case the trap density per volume is more important. Hence, the fraction of free electrons captured in the grain boundaries is higher for thinner films. These arguments allow to explain the variation of the carrier concentration versus film thickness. Finally, the electron mobility

is also observed to increase with the film thickness, which is attributed to an increase of effective conducting volume and a lower grain boundary scattering.

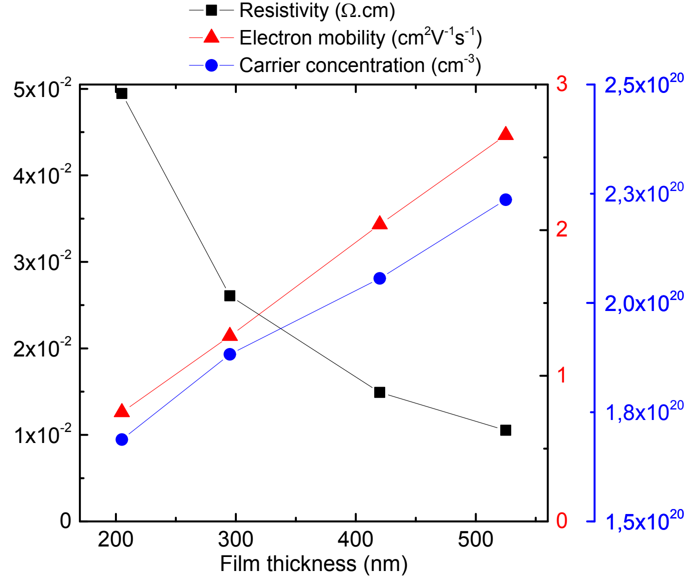

Figure 5 : Hall resistivity (-■-, left axis), electron mobility (-▲-, right axis) and carrier concentration (-●-, right axis) as a function of film thickness of AP-SALD ZnO:Al films deposited at 200 °C with various thicknesses.

5. Parameters used for conductivity modeling

In order to obtain a complete model for conductivity in highly doped ZnO:Al films, we used parameters reported in literature to describe scatterings due to impurities, phonon-electron interactions and dislocations, as shown in Table 1:

Table 1: Material parameters of ZnO:Al used for the simulation

Parameters [unit]	Values	References
Effective mass m_e divided by m_0 at the bottom of the conduction band	0.29	8
Nonparabolicity parameter C [eV^{-1}]	0.35 – 0.65	9,10,11
Static dielectric constant ε_s divided by ε_0	8.85	11
High-frequency dielectric constant ε_∞ divided by ε_0	3.66	11
Piezoelectric constant $P_\perp$	0.21	12
Energy of the longitudinal optical phonon [meV]	72.1	11
Average longitudinal elastic constant [GPa]	200	8
Deformation potential E_{ac} [eV]	3.8	8
Dislocation density N_{disl} [cm^{-2}]	1×10^{12}	13,14,15
Compensation ratio K	0.1 – 0.15	16

6. Effect of *C*, *K*, and N_t to the fits

Based on the previous work Young *et al,*[21] Look *et al,*[22] and T-Thienprasert *et al.*[38], we assumed that the nonparabolicity C can vary from 0.35 to 0.65 and the compensation ratio *K* can vary between 0.1 and 0.15 for a range of carrier concentrations in [$1.3\times10^{19} – 4.6\times10^{20}$ cm^{-3}]. Since *C* and *K* increase when the carrier density *n* increases, thus, as a first approximation, we assumed that *C* and *K* vary linearly with the Hall carrier density n_{Hall}.

In order to study the effect of C, K and N_t, we take the example of the sample prepared by RF sputtering shown in the manuscript, which have carrier density of 1.1 $\times 10^{20}$ cm^{-3} and mobility of 17.8 $cm^2V^{-1}s^{-1}$ at 300 K. In the manuscript, we showed that the best fit of experimental data to our AFTMM model occurs at $[C ; K ; N_t] = [0.5 ; 0.12 ; 3.9 \times 10^{13}$ $cm^{-2}]$. Figure 6 shows the variation of the mobility at 300 K when varying C, K and N_t around theirs standard values. We observed that varying C or K (up to 100 %) does not affect very much the mobility while a slight variation of N_t affect significantly the mobility. This affirmation becomes more valid when the carrier transport is mainly dominated by the grain boundaries. Additionally, this strong dependency of mobility versus the trap density at grain boundaries confirms the accuracy of our fitting results shown in table 3 in the manuscript.

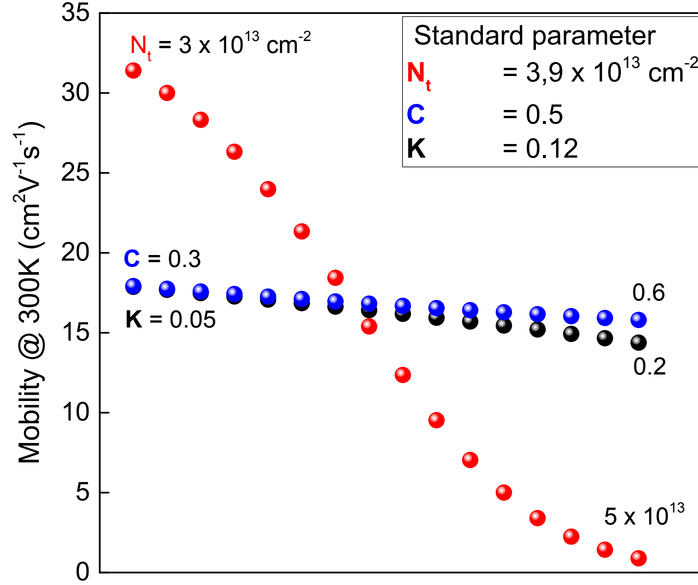

Figure 6: Effect of the nonparabolicity parameter C, the compensation ratio K and the trap density at grain boundaries N_t to the mobility at 300 K. L = 20 nm, n = 1.1 x 10^{20} cm^{-3}. Red: N_t varies from 3 x 10^{13} cm^{-2} to 5 x 10^{13} cm^{-2} while C and K are kept constant at their standard values. Blue: C varies from 0.3 to 0.6 while N_t and K are kept constant at their standard values. Black: K varies from 0.05 to 0.2 while N_t and C are kept constant at their standard values.

References

1 D. Muñoz-Rojas, V. H. Nguyen, C. Masse de la Huerta, S. Aghazadehchors, C. Jiménez and D. Bellet, *Comptes Rendus Phys.*, 2017, **18**, 391–400.
2 V. H. Nguyen, J. Resende, C. Jiménez, J.-L. Deschanvres, P. Carroy, D. Muñoz, D. Bellet and D. Muñoz-Rojas, *J. Renew. Sustain. Energy*, 2017, **9**, 021203.
3 T. I. Barry and F. S. Stone, *Proc R Soc Lond A*, 1960, **255**, 124–144.
4 J. F. Chang and M. H. Hon, *Thin Solid Films*, 2001, **386**, 79–86.
5 K. E. Lee, M. Wang, E. J. Kim and S. H. Hahn, *Curr. Appl. Phys.*, 2009, **9**, 683–687.
6 V. V. Titov, A. A. Lisachenko, I. K. Akopyan, M. E. Labzowskaya and B. V. Novikov, *J. Lumin.*, 2018, **195**, 153–158.
7 D. H. Zhang, *Mater. Chem. Phys.*, 1996, **45**, 248–252.
8 K. Ellmer, A. Klein, B. Rech and Ellmer-Klein-Rech, Eds., *Transparent conductive zinc oxide: basics and applications in thin film solar cells*, Springer, Berlin, 2008.
9 W. M. Kim, I. H. Kim, J. H. Ko, B. Cheong, T. S. Lee, K. S. Lee, D. Kim and T.-Y. Seong, *J. Phys. Appl. Phys.*, 2008, **41**, 195409.
10 D. L. Young, T. J. Coutts, V. I. Kaydanov, A. S. Gilmore and W. P. Mulligan, *J. Vac. Sci. Technol. Vac. Surf. Films*, 2000, **18**, 2978–2985.
11 V. Romanyuk, N. Dmitruk, V. Karpyna, G. Lashkarev, V. Popovych, M. Dranchuk, R. Pietruszka, M. Godlewski, G. Dovbeshko, I. Timofeeva, O. Kondratenko, M. Taborska, and A. Ievtushenko, *Acta Phys. Pol. A*, 2016, **129**, A-36-A-40.
12 X. Yang, C. Xu and N. C. Giles, *J. Appl. Phys.*, 2008, **104**, 073727.
13 A. Bikowski and K. Ellmer, *J. Appl. Phys.*, 2014, **116**, 143704.
14 D. C. Look, C. E. Stutz, R. J. Molnar, K. Saarinen and Z. Liliental-Weber, *Solid State Commun.*, 2001, **117**, 571–575.
15 L. Sagalowicz and G. R. Fox, *J. Mater. Res.*, 1999, **14**, 1876–1885.
16 D. C. Look, K. D. Leedy, L. Vines, B. G. Svensson, A. Zubiaga, F. Tuomisto, D. R. Doutt and L. J. Brillson, *Phys. Rev. B*, 2011, **84**, 115202.